Volume 19
Number 7
14 April 2026
Pages 2097–2386

Energy & Environmental Science

rsc.li/ees

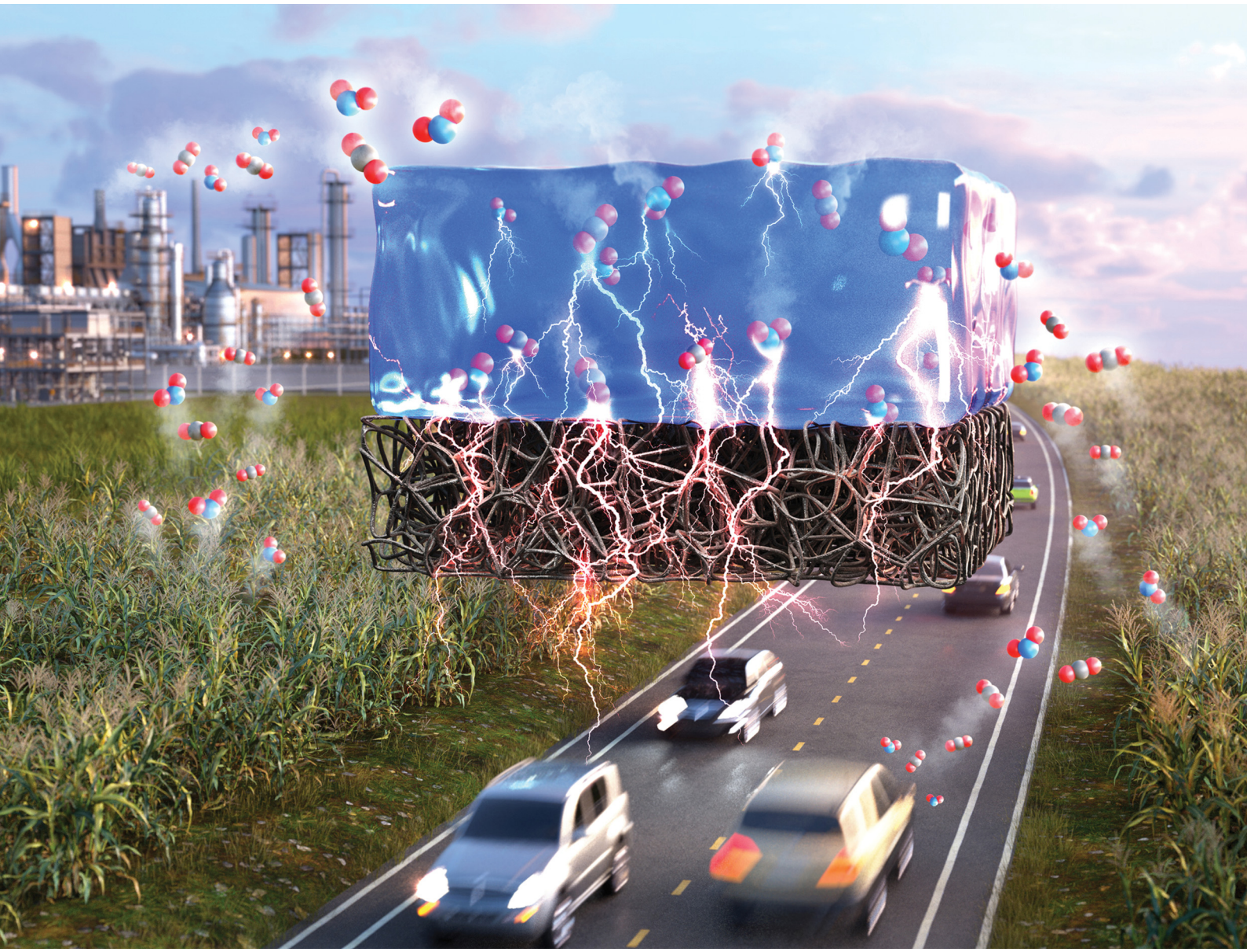

ISSN 1754-5706

ROYAL SOCIETY OF CHEMISTRY

PAPER
Tae Gwang Yun, Han Seul Kim, Ji-Soo Jang *et al.*
Electrical power generation from asymmetric greenhouse gas capture

Energy & Environmental Science

ROYAL SOCIETY OF CHEMISTRY

PAPER

View Article Online
View Journal | View Issue

Cite this: *Energy Environ. Sci.*, 2026, **19**, 2149

Electrical power generation from asymmetric greenhouse gas capture

Tae Gwang Yun,†*[b] Yejin Lee,†[ac] Joonchul Shin,†[d] Dong Ho Lee,[e] Min Taek Hong,[e] Seonghun Lee,[b] Sang-Joon Kim,[f] Hyun Ji Lee,[l] Jiwon Lee,[gh] Gyeongrok Min,[gi] Seunghyun Weon,[mn] Minho Choi,[mn] Ho Won Jang,[co] Han Seul Kim*[ejk] and Ji-Soo Jang*[p]

Received 9th November 2025,
Accepted 13th February 2026

DOI: 10.1039/d5ee06789h

rsc.li/ees

Capturing greenhouse gases (GHGs) while generating electricity offers a new paradigm for climate mitigation. Here, we report a GHG-driven energy harvesting system, termed a gas capture and electricity generator (GCEG), that directly converts the adsorption of NO_x and CO_2 into electrical power. The device integrates a carbon black-coated mulberry paper electrode with an asymmetrically dip-coated polyacrylamide hydrogel, enabling selective gas adsorption and voltage generation *via* modulation of the electrical double layer. Upon exposure to 50 ppm NO_2, the GCEG delivers 0.8 V and 55 μA, scaling to 3.8 V and 140 μA through series and parallel integration. Infrared spectroscopy and atomistic simulations reveal that hydrogen-bond-driven gas–hydrogel interactions govern the energy harvesting mechanism. By integrating gas capture and electricity generation within a single self-powered platform, this approach provides a scalable, low-energy pathway for mitigating multiple GHGs and offers a promising strategy toward carbon neutrality.

Broader context

Addressing the escalating impacts of climate change remains one of the most pressing global challenges. Despite continuous international efforts and advances in renewable energy and carbon-capture technologies, existing approaches still face intrinsic challenges such as high energy consumption, low selectivity, and complicated processing routes. In this work, we propose a gas capture and electricity generator (GCEG) system capable of directly capturing greenhouse and toxic gases while converting their adsorption energy into usable electricity. The GCEG employs a hydrogel-coated, carbon-based electrode that selectively adsorbs NO_x and CO_2 and transforms the resulting surface potential into electrical power, establishing an energy-generating carbon-mitigation platform. In particular, chemical functionalization of the hydrogel enables electricity generation during NO_x adsorption, while chemical modification of the carbon materials allows power generation from CO_2 capture as well. This study moves beyond conventional adsorption-based carbon-reduction strategies by introducing an integrated system that simultaneously performs gas capture and energy conversion. The proposed approach opens a pathway toward a self-powered and sustainable platform that not only removes harmful gases but also contributes to carbon neutrality through energy generation.

[a] *Electronic and Hybrid Materials Research Center, Korea Institute of Science and Technology (KIST), Seoul 02792, Republic of Korea*
[b] *Department of Molecular Science and Technology, Ajou University, Suwon 16499, Republic of Korea*
[c] *Department of Materials Science and Engineering, Research Institute of Advanced Materials, Seoul National University, Seoul 08826, Republic of Korea*
[d] *Advanced Bio and Healthcare Materials Research Division, Korea Institute of Materials Science (KIMS), Changwon, Republic of Korea*
[e] *Department of Advanced Materials Engineering, Chungbuk National University, Cheongju 28644, Republic of Korea*
[f] *Korea Department of Materials Science and Engineering, Chungnam National University, Daejeon 34134, Republic of Korea*
[g] *Center for Climate and Carbon Cycle Research, Korea Institute of Science and Technology (KIST), Seoul 02792, Republic of Korea*
[h] *Division of Energy & Environment Technology, KIST School, University of Science and Technology, Seoul 02792, Republic of Korea*
[i] *Department of Materials Science and Engineering, Korea University, Seoul 02841, Republic of Korea*
[j] *Department of Urban, Energy, Environmental Engineering, Chungbuk National University, Cheongju 28644, Republic of Korea*
[k] *Advanced Energy Research Institute, Chungbuk National University, Chungdae-ro 1, Seowon-Gu, Cheongju, Chungbuk 28644, Republic of Korea*
[l] *CO2 & Energy Research Center, Korea Research Institute of Chemical Technology (KRICT), Daejeon 34114, Republic of Korea*
[m] *School of Health and Environmental Science & Department of Health and Safety Convergence Science, Korea University, Seoul 02841, Republic of Korea*
[n] *Transdisciplinary Major in Learning Health Systems, Graduate School, Korea University, 145 Anam-Ro, Seoul 02841, Republic of Korea*
[o] *Advanced Institute of Convergence Technology, Seoul National University, Suwon 16229, Republic of Korea*
[p] *SKKU Advanced Institute of Nanotechnology and Department of Nanoengineering, Sungkyunkwan University, Suwon 16419, Republic of Korea*
† Shares equal contribution.

Introduction

Accelerating climate change represents one of the most critical global challenges, demanding innovative strategies to achieve net-zero greenhouse gas (GHG) emissions.[1,2] Decades of cumulative emissions have already led to a steady rise in atmospheric GHG concentrations, intensifying the urgency of mitigation efforts. Thus, suppressing future emissions alone is insufficient; technologies capable of actively removing and reducing already-emitted GHGs are indispensable. The six major GHGs, carbon dioxide (CO_2),[3] methane (CH_4), nitrous oxide (N_2O), hydrofluorocarbons (HFCs), perfluorocarbons (PFCs), and sulfur hexafluoride (SF_6), have been identified as primary contributors to global warming.[4] Among them, CO_2 is the most significant due to its massive emissions from fossil fuel combustion and environmental destruction. In addition, nitrogen oxides (NO_x), extensively released from industrial processes, vehicle exhausts, and agricultural activities, contribute to ozone formation under solar irradiation, thereby exerting a substantial impact on climate change.[5,6]

To address these challenges, extensive efforts have focused on developing carbon capture, utilization, and storage (CCUS) technologies.[7] Conventional CCUS approaches, such as amine adsorption and calcium looping, capture CO_2 and subsequently release it under high-temperature and high-pressure conditions for reuse or long-term storage.[8] Captured CO_2 can further be converted into carbon-based organic materials or petrochemicals such as olefins, naphtha, and aromatics, or utilized as synthetic gas for fuels. However, these processes are highly energy-intensive, requiring substantial thermal energy as well as expensive noble-metal catalysts for CO_2 conversion. Furthermore, CCUS technologies remain largely constrained to CO_2, lacking the flexibility to address other critical GHGs such as NO_x. Consequently, CCUS, while powerful, faces intrinsic limitations, including high energy consumption, catalyst dependence, and limited applicability to diverse GHGs.

Given these limitations, approaches are needed that can selectively capture GHGs and simultaneously convert them into useful forms of energy without additional thermal energy or catalysts. Beyond simple capture, the direct utilization of GHGs as an energy source offers a transformative pathway toward sustainable climate mitigation. Recent advances in hydrovoltaic and moisture-based nanogenerators, which generate electricity *via* asymmetric adsorption of ions and molecules in water, demonstrate the potential of adsorption-driven energy harvesting[9] (Table S1). However, these water-based systems face inherent drawbacks, including long-term water consumption, evaporation-induced instability, and corrosion. Considering water's critical ecological role, such limitations hinder large-scale sustainability. Therefore, utilizing GHGs themselves as an energy reservoir presents a paradigm that can overcome the shortcomings of water-based systems while directly contributing to net-zero emissions.

Herein, we report for the first time a simple and robust gas capture and electricity generator (GCEG) system, which simultaneously captures GHGs and generates electricity. The device is based on a conductive carbon/cellulose backbone asymmetrically coated with a hydrogel layer, enabling the selective adsorption of NO_x and CO_2 from the surrounding atmosphere while producing a direct voltage and current output. Upon exposure to 50 ppm NO_2, the GCEG exhibits an open-circuit voltage (V_{OC}) of $\sim$0.8 V and a short-circuit current (I_{SC}) of $\sim$80 μA, sustained by the reversible adsorption–desorption dynamics of gas molecules. Atomistic simulations confirmed that the energy generation mechanism originates from unique electronic interactions between NO_2 molecules and the hydrogel interface. Moreover, the voltage output remains stable for up to 24 hours under continuous gas flow and demonstrates robust reproducibility. As a proof of concept, the device successfully harvested electricity from NO_x emitted during agricultural microbial decomposition. Importantly, the scalability of the GCEG with device arrays was demonstrated, highlighting its potential for practical deployment. By harnessing captured GHGs directly as an energy source, this innovative approach not only contributes to emission reduction but also introduces a paradigm shift in transforming harmful GHGs into valuable and sustainable electricity.

Results and discussion

Design and working principle of the gas capture and electricity generator (GCEG)

We demonstrate a strategy that integrates gas capture and electricity generation within a single system. As a proof of concept, we present the GCEG, a self-powered device that selectively captures NO_x and CO_2 while producing electrical output (Fig. 1). The GCEG incorporates a polyacrylamide (PAM) hydrogel layer that selectively adsorbs GHG molecules, along with a mulberry paper (cellulose-based natural fiber) electrode coated with carbon black (CB) nanoparticles, which generates a potential difference and current (Fig. S1). Notably, the PAM hydrogel layer adopts a "Janus" structure, with the coating applied to only one half of the fiber electrode, establishing a potential difference between the two ends of the electrode (Fig. 1a). A detailed description of the device fabrication and materials is provided in the Methods section.

Electricity generation in the GCEG system arises from a cation exclusion effect triggered by the selective adsorption of gas molecules within the PAM hydrogel. The mechanism proceeds as follows: (i) gas molecules that interact strongly with PAM amide groups (–$CONH_2$) are selectively captured. NO_2 molecules, in particular, act as strong electron acceptors with high electron affinity and are well-known oxidizing gases, thereby enhancing their interaction with polar functional groups in the hydrogel and increasing their affinity for the hydrogel matrix.[10,11] (ii) These interactions induce a spatial redistribution of electron density, leading to partial electron depletion around the amide groups. The induced partial positive charge promotes cation exclusion from the hydrogel and drives the migration of cations toward the electrode surface.[12] (iii) The excluded cations subsequently adsorb onto nanostructured carbon surfaces, whose

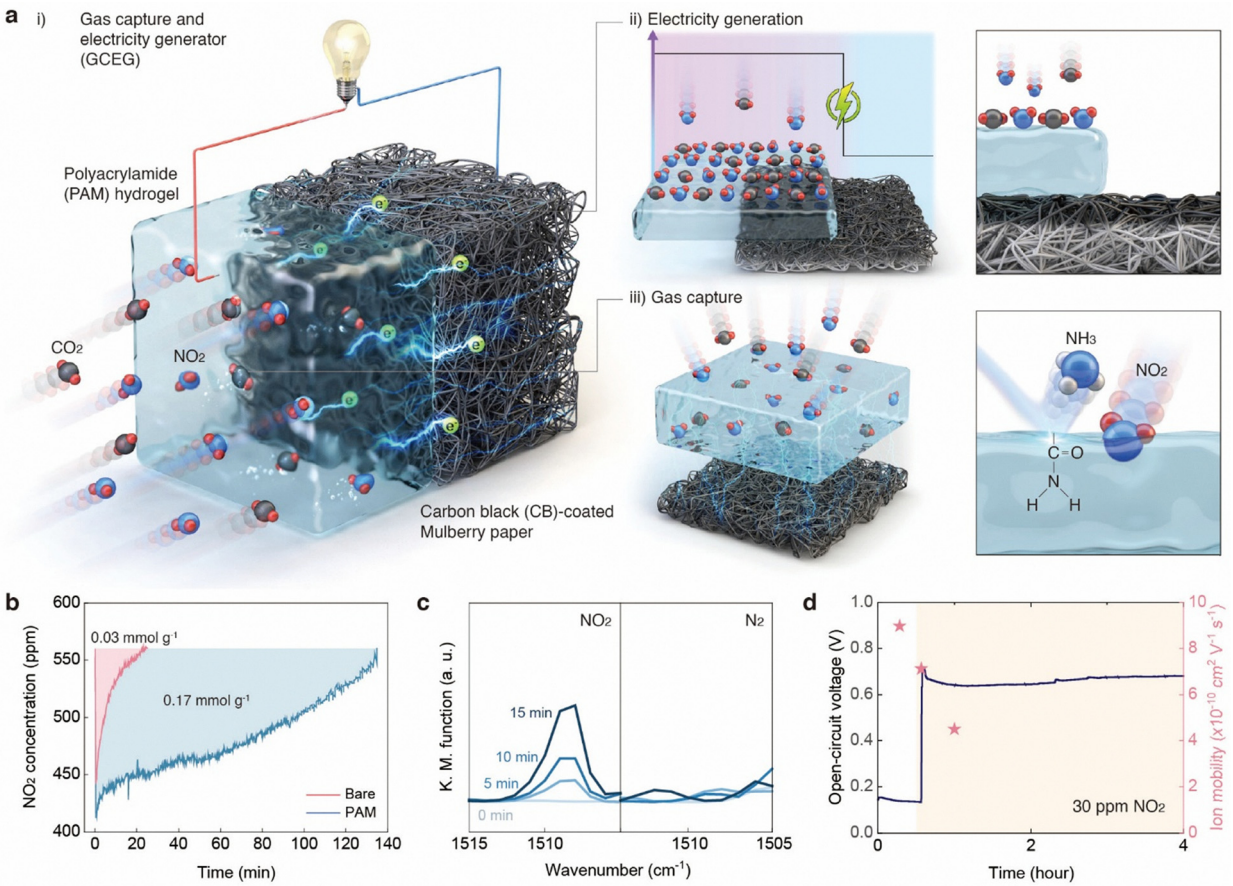

Fig. 1 The gas capture and electricity generator (GCEG) and its main properties. (a) Schematic illustration of the GCEG device, featuring an asymmetric structure with a PAM hydrogel coating on one half of the CB-coated mulberry paper. The device enables electricity generation and gas capture. (b) Adsorption capacity of the PAM hydrogel evaluated under continuous 560 ppm NO_2 exposure. (c) *In situ* diffuse reflectance infrared Fourier transform spectroscopy (DRIFTS) spectra of the hydrogel after exposure to 1000 ppm NO_2 and N_2 for 15 min at room temperature. (d) Time-dependent V_{OC} of the GCEG under continuous 30 ppm NO_2 exposure at 30% relative humidity (RH), and the corresponding ion mobility changes upon NO_2 exposure as determined by *in situ* electrochemical impedance spectroscopy (EIS).

integration with mulberry paper maximizes cation adsorption capacity.[13] Notably, the Janus electrode design induces an asymmetric cation distribution, generating a potential difference that drives electron flow and enables electricity generation. To validate the proposed selective gas adsorption mechanism of the GCEG, the gas adsorption capacity was quantified through controlled gas uptake measurements (Fig. S2). The adsorption capacity was calculated using a mass balance equation derived from the breakthrough curve showing changes in concentration (Fig. 1b and Discussion S1). The CB-coated mulberry paper exhibited an NO_2 adsorption capacity of 0.03 mmol g^{-1}, whereas integration with the PAM hydrogel increased the NO_2 capacity to 0.17 mmol g^{-1}. This enhancement indicates that incorporating the PAM hydrogel induces asymmetric NO_2 adsorption between the hydrogel layer and the CB-coated mulberry paper. Although the NO_2 adsorption capacity of the present GCEG is lower than that of state-of-the-art sorbents optimized solely for gas capture (Table S2), the primary significance of this work lies in demonstrating a passive device concept that directly converts gas adsorption into electrical energy.

To further investigate the selective NO_2 gas adsorption mechanism in the PAM hydrogel layer, molecular interactions were examined using *in situ* diffuse reflectance infrared Fourier transform spectroscopy (*in situ* DRIFTS) (Fig. 1c and Fig. S3). Infrared (IR) spectra of the PAM hydrogel, recorded 15 min after exposure to 1000 ppm NO_2 or N_2 under dry conditions, were baseline-corrected using the initial hydrogel spectrum to minimize background interference. A peak at 1600–1500 cm^{-1}, attributed to NO_2 stretching,[14,15] intensified with prolonged NO_2 exposure, whereas no distinct vibrational band was observed under N_2 flow (Fig. 1c). This observation indicates strong dipole–dipole interactions and hydrogen bond formation between the amide groups of the hydrogel and NO_2 molecules,[16–18] accompanied by additional weak van der Waals interactions. These interactions sustain voltage generation as long as the NO_2 concentration is maintained. When the gas is supplied at a stable concentration, the output voltage rises sharply until it reaches a saturation level and then remains steady over time. For example, at a constant 30 ppm NO_2, the voltage rose sharply to a saturation point and remained stable for 4 h (Fig. 1d). The maximum voltage corresponds to an equilibrium between adsorbed NO_2 on the hydrogel and the surrounding atmosphere, after which the output remains constant. Notably, additional

long-term stability tests demonstrate that the saturated voltage can be sustained for more than 24 h without noticeable degradation (Fig. S4), and repeated adsorption–desorption cycling tests over 15 cycles show stable and reproducible voltage and current responses (Fig. S5). The cycling stability of the GCEG was evaluated based on the ratio of the response amplitudes between the initial and final cycles. The response amplitude, defined as the difference between the baseline and response voltages in each cycle, decreased slightly from 0.70 V (first cycle) to 0.665 V (final cycle), corresponding to a response retention of 95.0%. Furthermore, the device maintains reliable voltage generation under both low- and high-temperature conditions, confirming the robustness of the gas-induced electricity generation mechanism across a wide range of environmental conditions (Fig. S6).

The strong interaction between NO_2 and the PAM hydrogel induces electron density redistribution, leading to a cation exclusion effect. To examine its influence on ion transport, we measured the ionic conductivity and mobility of the hydrogel using *in situ* electrochemical impedance spectroscopy (*in situ* EIS) (Fig. 1d and Fig. S7). Ionic mobility (μ) was calculated from the Nernst–Einstein equation:

$$\mu = \frac{e\lambda^2\omega_2}{k_B T}$$

where μ represents the ion mobility ($cm^2\ V^{-1}\ s^{-1}$), λ is the thickness of the electrical double layer (EDL) (cm), ω_2 is the angular frequency corresponding to the minimum in the imaginary impedance (s^{-1}), e is the elementary charge, k_B is the Boltzmann constant, and T is the absolute temperature. Upon exposure to 50 ppm NO_2, gradual hydrogen-bond formation between NO_2 and the amide groups reduced ion mobility from 8.97 to $7.12 \times 10^{-10}\ cm^2\ V^{-1}\ s^{-1}$, reaching $4.5 \times 10^{-10}\ cm^2\ V^{-1}\ s^{-1}$ at saturation. When the gas flow was stopped, mobility recovered to its initial value, confirming that NO_2 adsorption reversibly inhibits ion movement, a phenomenon attributed to the strong intermolecular interactions between the NO_2 gas and the hydrogel (Fig. S8). This reversible suppression of ion mobility strengthens the cation exclusion effect, driving cations toward the electrode surface and contributing to potential generation.

Atomistic origin of GCEG operation

To gain molecular-level insight into the gas-selective cation exclusion mechanism driving power generation in the GCEG system, we performed multiscale simulations combining molecular dynamics (MD) and density functional theory (DFT). Two representative models were prepared: dry and fully-hydrated (Fig. 2a) PAM hydrogels to analyze the adsorption-induced power generation behavior of five distinct gas species: NO_2, NO, CO_2, NH_3, and H_2. Projected density of states (PDOS) analysis of the hydrated system classifies the gases into three different types (Fig. 2b). Type A gases (NO_2 and NO) are characterized by distinct molecular peaks (E_P) located near the Fermi energy level (E_F), enabling efficient electron transfer to the PAM hydrogel. The type B gas (CO_2) retains identifiable peaks, but these are located far from the E_F, leading to weaker charge transfer. Meanwhile, type C gases (NH_3 and H_2) exhibit negligible gas-specific peaks hybridized with H_2O through hydrogen bonding networks. This indicates minimal electronic interaction with the hydrogel matrix but a much stronger interaction with water.

Notably, such gas-specific interactions are greatly intensified by hydration. Relative to the dry condition, hydration markedly decreases the E_P–E_F value, narrowing the gap between the gas molecular states and E_F by consequently lowering the energy barrier for charge transfer (Fig. 2c and Fig. S9): the energy gaps decrease from 0.67 eV to 0.44 eV for NO_2, from 0.31 eV to 0.11 eV for NO, and from 3.47 eV to 2.77 eV for CO_2. This hydration-assisted modulation leads to distinct changes in the net electron density of the PAM hydrogel. Type A gases act as strong electron donors to the hydrogel, while type C gases behave as either an electron acceptor (H_2) or a weak donor (NH_3) through hydrogen bonding with water rather than with the hydrogel (Fig. 2d and Fig. S10). Meanwhile, type B gas (CO_2) exhibits moderate electron transfer by interacting with both the hydrogel and surrounding water molecules. The effect of charge transfer is directly reflected in the downward shift of E_F (ΔE_F) upon gas adsorption (Fig. 2e and Fig. S9). The magnitude of ΔE_F follows the order type A (-2.72 eV and -1.53 eV for NO_2 and NO, respectively) $>$ type B (-1.03 eV for CO_2) $>$ type C (-0.20 eV and -0.28 eV for NH_3 and H_2, respectively). Importantly, despite its intrinsically low solubility under hydrated conditions, type B gas (CO_2) produces a moderate E_F shift when modeled in a fully dissolved state. This result implies that CO_2 could also contribute significantly to voltage generation in environments where its solubility is enhanced.

Distinct molecular peaks near the E_F, along with the E_F shift, indicate a spatial redistribution of electron density within the hydrogel. The gas-specific E_F modulation reflects gas-dependent electronic interactions and the resulting tendency for cation exclusion. When the PAM hydrogel contacts the CB-coated mulberry paper electrode, larger E_F shifts promote greater charge displacement toward the electrode, whereas smaller shifts induce weaker transfer. This effect manifests as a gas-specific gating behavior. Within the Janus electrode configuration of the GCEG system, the hydrogel-coated and uncoated sides therefore experience different potential responses depending on gas type, giving rise to a measurable electrostatic potential difference. This potential difference translates into the output voltage of the device and serves as the driving force for current flow. The sequential mechanism—selective gas adsorption, hydration-assisted E_F modulation, charge redistribution, and Janus-induced output voltage generation—is illustrated in Fig. 2f. Type A gases, which induce the largest E_F shifts, yield the strongest cation exclusion, followed by the intermediate response of type B and the negligible response of type C. These results suggest that optimizing the PAM layer and electrode design could extend electricity generation to include selective adsorption of type B gases (CO_2).

Electrical output characteristics of GCEG

To validate the integration of GHG capture and power generation, the electricity generation performance of the GCEG was

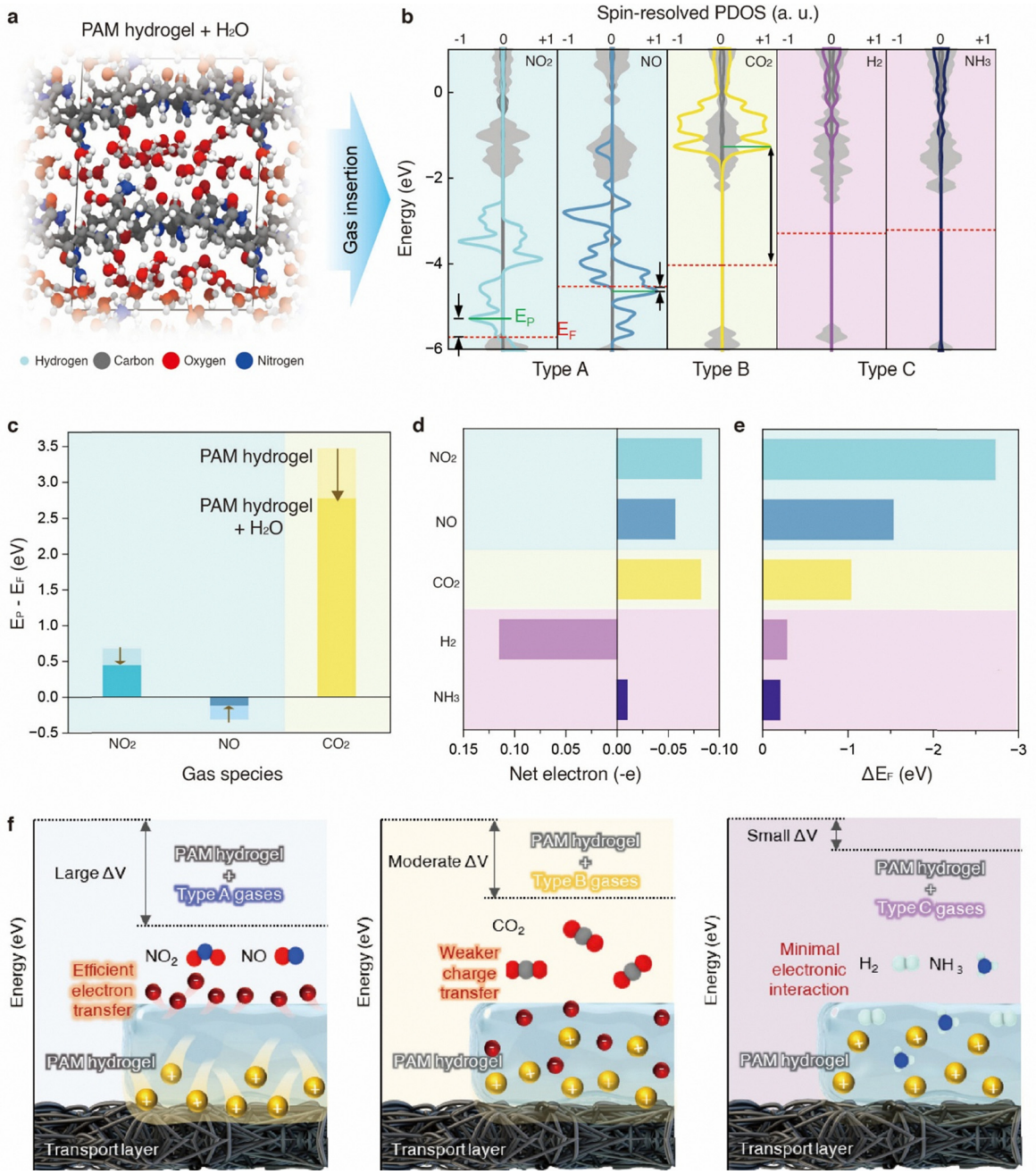

Fig. 2 Atomistic simulation results for the GCEG systems upon adsorption of gas species. (a) An atomistic model of the hydrated PAM hydrogel. (b) Spin-resolved PDOS plots for type A (NO_2 and NO), type B (CO_2), and type C (H_2 and NH_3) molecules. Positive and negative values indicate the magnitude of DOS for up and down electronic spins, respectively. In the plots, the light gray shading, dark gray line, and colored lines denote the hydrogel, water, and the adsorbed gas species, respectively, while the red dashed and green dotted lines mark the Fermi level (E_F) and the nearest molecular peak (E_P). (c) Summary of E_P–E_F values for type A and type B molecules; lighter and darker bars indicate values before and after hydration of the PAM hydrogel, respectively. (d) Change in the net electron count associated with each gas molecule within the system and (e) corresponding ΔE_F of the system under hydrated and gas-adsorbed conditions. (f) Schematic energy diagrams of GCEG output voltage generation for type A (left), type B (center), and type C (right) gases with large, moderate, and small ΔV, respectively.

evaluated (Fig. 3). Specifically, the correlation between electrical output and factors such as gas concentration and humidity was established to maximize power generation efficiency. Measurements were conducted in a controlled chamber using a source meter, with the gas concentration and humidity precisely regulated by mass flow controllers (MFCs) (Fig. S11). The output voltage originates from the EDL formed by the adsorption of water molecules and ions from the asymmetric hydrogel onto the CB surface,[9] enabling a potential difference of $\sim$0.1 V even at 0% RH. Power generation tests were thus performed by introducing gas under constant RH conditions. As shown in Fig. 3a, the output of the GCEG began to rise at

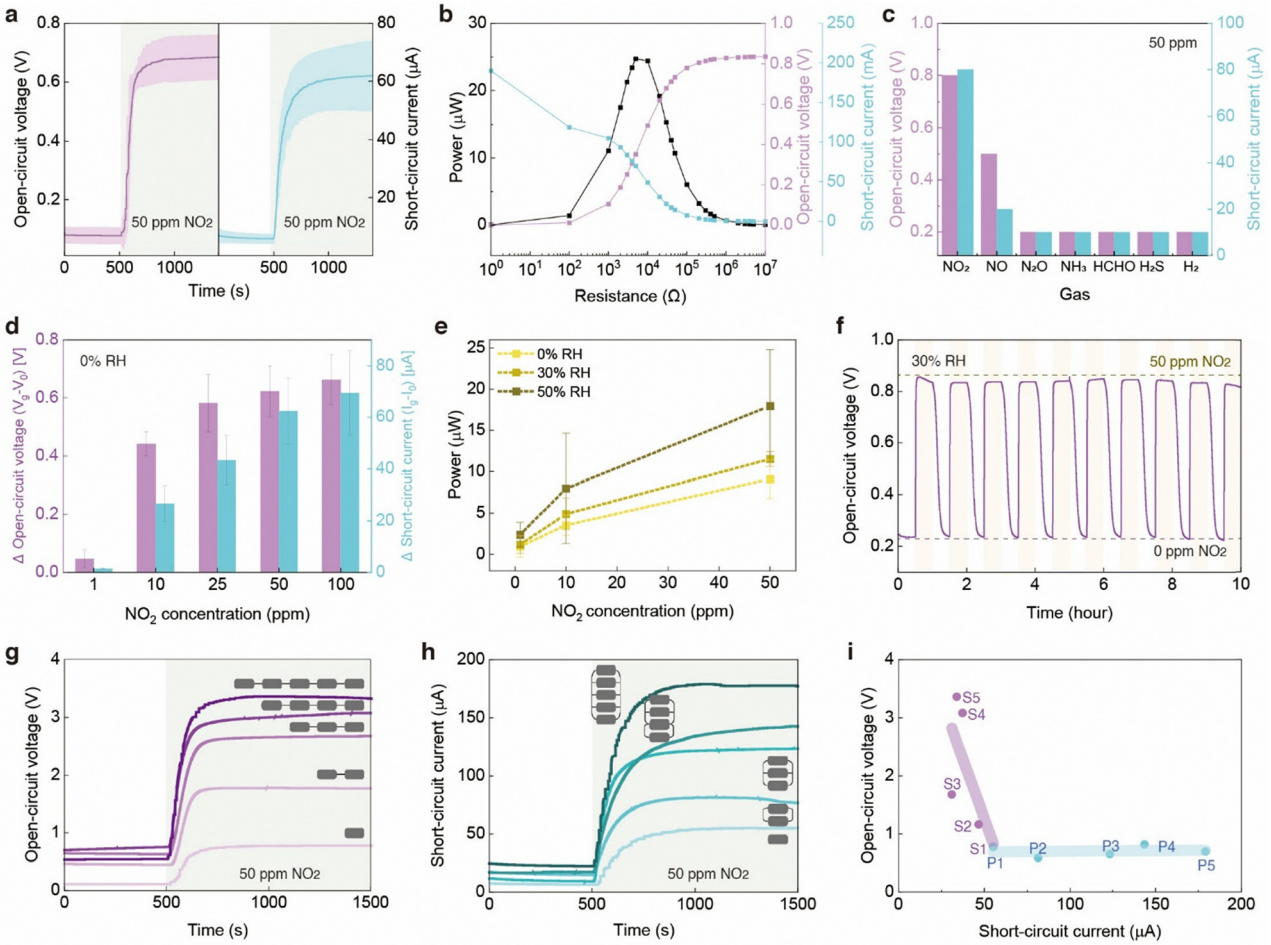

Fig. 3 Electrical performance of the GCEG. (a) Measured V_{OC} and I_{SC} profiles of the GCEG (20 kΩ load) under 50 ppm NO_2 exposure at 0% RH. (b) Variation of V_{OC}, I_{SC}, and power output with external load resistances ranging from 1 Ω to 10 MΩ under 50 ppm NO_2 exposure at 50% RH. (c) Gas selectivity of the GCEG evaluated by comparing the maximum V_{OC} and I_{SC} under 50 ppm exposure to different gases at 0% RH. (d) Dependence of output voltage and current on NO_2 concentration (0–100 ppm) at 0% RH. (e) Variation of power output with NO_2 concentration and RH. (f) Long-term stability of the GCEG under cyclic adsorption–desorption of 50 ppm NO_2 at 30% RH. (g) Voltage and (h) current output from the five GCEG devices connected in series and parallel, respectively. (i) Enhanced output performance achieved by connecting multiple GCEG devices in series or parallel configurations under 50 ppm NO_2 exposure at 0% RH.

500 s upon injection of 50 ppm NO_2. Subsequently, with the continuous NO_2 inflow, the adsorption reaction at the hydrogel interface reached equilibrium, resulting in a maximum output voltage of 0.8 V and a current of 55 μA. To evaluate the maximum power output, a variable resistor (10 kΩ–10 MΩ) was connected to the external circuit (Fig. 3b). The power density (P) was calculated as:

$$P = (I^2R)/A$$

where I denotes the output current that varies with the external load, R denotes the load resistance, and A represents the area of the GCEG. As R increased, the voltage increased while the current decreased, yielding a maximum power of 24 μW for a GCEG (3×6 cm^2) at 10 kΩ under 50 ppm NO_2 at 50% RH (Fig. 3b).

To experimentally validate the atomistic power generation mechanism proposed for the GCEG system, we examined the correlation between gas type and the resulting electrical output (Fig. 3c). Type A gases (NO_2 and NO) generated high voltage and current due to their large E_F shifts, which reinforce cation exclusion and amplify the potential difference across the Janus electrodes. In contrast, type C gases (NH_3 and H_2) showed negligible electrical output, as their weak interaction with the PAM hydrogel produced minimal E_F modulation and cation exclusion, despite strong interactions with water.

The operation mechanism of the GCEG system was further verified by correlating gas adsorption, hydrogel water content, and power generation. Voltage and current were measured under 0% RH while varying NO_2 concentrations from 1 to 100 ppm (Fig. 3d). Increasing NO_2 concentration enhanced adsorption within the hydrogel, thereby reinforcing the cation exclusion effect and elevating the maximum output voltage and current. Saturation of adsorption sites led to thermodynamic equilibrium and peak power output, indicating that reversible intermolecular interactions between NO_2 molecules and the PAM hydrogel govern both adsorption selectivity and electricity

generation. Notably, an electrical response was observed even at concentrations as low as 0.5 ppm, indicating the high sensitivity of the device (Fig. S12). Experiments conducted at a constant gas concentration under varying RH (0%, 30%, and 50%) show that increasing RH enhances the power output of the device (Fig. 3e and Fig. S13). Higher hydrogel water content promoted ion and water transport, further amplifying the cation exclusion effect. At elevated RH, excessive moisture weakens the control of the hydrogel-enabled asymmetric adsorption, leading to increased variability in device performance and consequently larger error bars. These variations reflect humidity-induced fluctuations rather than statistically meaningful deviations from the overall monotonic trend. When RH exceeds 80%, however, a slight decrease in power output is observed (Fig. S14), which is attributed to the loss of a fully dry region and the resulting reduction in contrast between the dry and wet regions. Collectively, these results indicate that electricity generation in the GCEG originates from gas-induced charge redistribution and electrostatic potential modulation that reinforce cation exclusion, and that strengthening this asymmetry directly enhances device performance.

A distinctive feature of the GCEG is its switchable power generation, which arises from the reversible adsorption and desorption of incoming gas molecules. To verify the on–off power generation behavior, the output voltage was monitored for 10 h under alternating injections of 50 ppm NO_2 and air (Fig. 3f). Under continuous NO_2 supply, the maximum power output was maintained at a stable level, whereas air injection that reduced the NO_2 level to 0 ppm restored the output voltage to its initial state. When water or an amine solution was impregnated into the carbon instead of the hydrogel, reversible voltage on/off characteristics were not observed (Fig. S15). This reversible response highlights the dynamic redistribution of electron density within the hydrogel, indicating that the power generation characteristics of the GCEG are governed by gas adsorption–desorption equilibria. In addition, the output performance of the GCEG can be systematically enhanced through serial and parallel configurations (Fig. 3g and h). A series connection of five devices yielded a maximum output voltage of 3 V, while a parallel connection produced a maximum current of approximately 160 μA. These results demonstrate that even simple circuit-level integration enables effective amplification of the output performance (Fig. 3i and Fig. S16). Furthermore, connecting additional GCEG devices allows the generation of higher power outputs as required, thus facilitating straightforward scale-up.

Extension of gas-driven power generation *via* the CO_2–amine reaction

As a step toward establishing the GCEG as a practical GHG mitigation technology, we further introduced a CO_2-adapted architecture that couples selective adsorption of CO_2 with electricity generation, thereby extending the scope of the GCEG (Fig. 4a). Unlike polar gases such as NO_2 and NH_3, nonpolar CO_2 has low chemical reactivity and does not form hydrogen bonds with the PAM hydrogel.[3] However, due to its moderate solubility in water, a portion of CO_2 dissolves into the hydrogel, where it reacts with water to produce bicarbonate (HCO_3^-) and protons (H^+).[19,20] The resulting proton migration generates a modest voltage under 30% CO_2 exposure (Fig. 4b). This electrochemical response, originating from CO_2 dissolution, does not fully recover upon air reintroduction and exhibits only a limited spontaneous reversibility (Fig. S17).

To enhance the GCEG response to CO_2, an amine solution consisting of monoethanolamine (MEA, primary amine) and diethanolamine (DEA, secondary amine) was applied asymmetrically to the electrode surface, leaving the PAM hydrogel region unmodified. In aqueous environments, CO_2 reacts with both primary and secondary amines *via* well-established pathways, including the zwitterion mechanism and subsequent carbamate or bicarbonate formation. In both cases, CO_2 initially forms a zwitterionic intermediate, followed by proton transfer, resulting predominantly in ammonium carbamate species for primary and secondary amines. Accordingly, in the presence of CO_2, the amines form carbamate or bicarbonate species, releasing protons and thereby amplifying interfacial reactivity.[19] Under air flow in a cross-polarity electrode configuration, an initial output voltage was generated by EDL formation at the amine–CB interface (Fig. 4c). Upon switching the atmosphere to 30% CO_2, this voltage progressively decreased, consistent with the reaction pathway described in the following equations:

$$\text{Primary amine (MEA): } 2RNH_2 + CO_2 \rightarrow RNHCOO^- + RNH_3^+$$

$$\text{Secondary amine (DEA): } 2R_2NH + CO_2 \rightarrow R_2NCOO^- + R_2NH_2^+$$

Through these reactions, the amine solution forms carbamate ($RNHCOO^-$ or R_2NCOO^-) or bicarbonate (HCO_3^-) species. The formation of these anionic species is accompanied by proton (H^+) generation, which initially contributes to EDL formation at the amine–CB interface. However, as the local concentration of H^+ near the CB surface decreases through neutralization or electrostatic displacement by the accumulated anions, the interfacial energy gradually approaches that of the bare CB without amine treatment. Consequently, the EDL-induced surface charge potential, which was initially modulated by proton enrichment, progressively returns toward its baseline level. This restoration attenuates the potential gradient between amine-modified and unmodified regions, thereby leading to a measurable decline in overall voltage output.

Building upon these findings, the system was further evaluated with the DEA solution as the cathode and the PAM hydrogel as the anode under a 10% CO_2 atmosphere (Fig. 4d). Comparable output characteristics were observed for the MEA-based system, as detailed in the SI (Fig. S18). CO_2 exposure maximized the potential difference between the electrodes, markedly increasing the output voltage. This phenomenon arises from increased surface energy at the amine interface due to anion accumulation, contrasted with decreased surface energy at the PAM hydrogel interface, thereby amplifying the potential gradient. Unlike NO_2-driven processes in the GCEG,

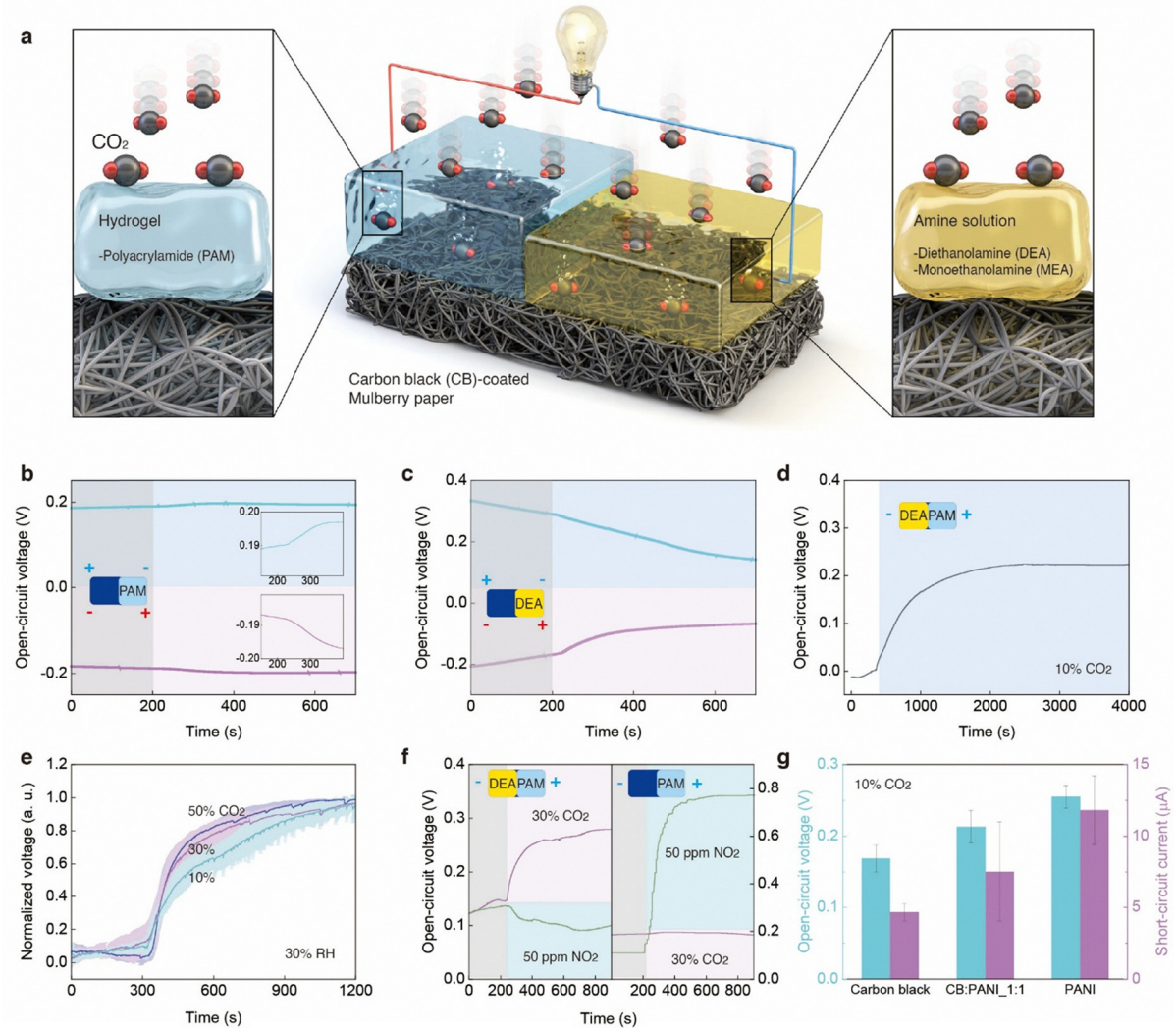

Fig. 4 Electrical performance of the modified GCEG under CO_2 exposure. (a) Schematic of the modified GCEG incorporating an amine solution (diethanolamine (DEA) or monoethanolamine (MEA)), featuring an asymmetric structure with a hydrogel coating on one half of the CB-coated mulberry paper and an amine solution coating on the other half. (b) V_{OC} profiles of the original GCEG under 30% CO_2 exposure in air with different electrode configurations. (c) V_{OC} profiles of the modified GCEG with DEA (DEA–GCEG) under 30% CO_2 exposure in air with different electrode configurations. (d) Maximum electrical output of the DEA–GCEG under 10% CO_2 exposure. (e) Normalized V_{OC} profiles of the DEA–GCEG at various CO_2 concentrations. (f) Comparison of V_{OC} for the GCEG and DEA–GCEG under 30% CO_2 exposure and 50 ppm NO_2 exposure. (g) Comparison of V_{OC} and I_{SC} for the DEA–GCEG devices with different active materials under 10% CO_2 exposure at 30% RH.

CO_2 reactions in this system are irreversible at ambient temperature; air purging cannot induce desorption. This non-recoverable response arises from the exothermic amine–CO_2 reaction, whose reversal is thermodynamically unfavorable without thermal input.

To elucidate the influence of CO_2 concentration on output voltage, voltage profiles were measured under 10%, 30%, and 50% CO_2 (Fig. 4e). The saturation voltage was nearly constant across concentrations, but the time to reach saturation decreased as CO_2 levels increased. Given the 1 : 1 stoichiometry between CO_2 and amines, saturation occurs once all accessible amine sites on the CB surface have reacted. The resulting amine–CO_2 adduct is highly stable, inhibiting the reverse reaction at ambient temperature. Consequently, even at low CO_2 concentrations, sustained CO_2 exposure ultimately consumes all amine groups, yielding the same saturation voltage. This behavior substantiates that the output voltage is governed by the irreversible amine–CO_2 chemical reaction under ambient conditions (Fig. S19). Although minor contributions from reversible physical adsorption processes, such as those associated with the PAM hydrogel, can lead to partial regeneration of the electrical response (Fig. S20), the realization of a fully regenerable system remains limited within the current device architecture.

The CO_2 gas adsorption capacities of the GCEG were also evaluated. Consistent with the previous section, the CO_2 adsorption capacities of the CB-coated mulberry paper, PAM hydrogel, and DEA–GCEG were quantified (Fig. S21 and Discussion S1). The measured CO_2 adsorption capacities were 2.404, 9.721, and 25.793 mmol g^{-1} for the CB-coated mulberry

paper (bare), PAM hydrogel, and DEA–GCEG, respectively, showing a progressive increase with the addition of adsorbents.

The voltage generation characteristics of the original GCEG system and the DEA–GCEG were compared under exposure to 50 ppm NO_2 and 30% CO_2 (Fig. 4f). The original GCEG responded strongly to NO_2 but negligibly to CO_2, whereas the DEA–GCEG showed the opposite behavior. The introduction of selective adsorption sites, hydrogels for NO_2 and amines for CO_2, therefore enables controlled energy harvesting from multiple GHGs. To further demonstrate material versatility, we incorporated CB with the conductive polymer polyaniline (PANI), both in pure form and as PANI–carbon composites (Fig. 4g and Fig. S22). These configurations maintain CO_2-responsive power generation (Fig. S23), highlighting the adaptability of the GCEG platform through hydrogel–polymer integration.

Potential applications of the GCEG

To demonstrate the scalability and practical applicability of the GCEG, we constructed an array system as shown in Fig. 5a. Up to 25 GCEG devices were placed in a gas chamber, where the gas concentration and flow rate were precisely controlled by the

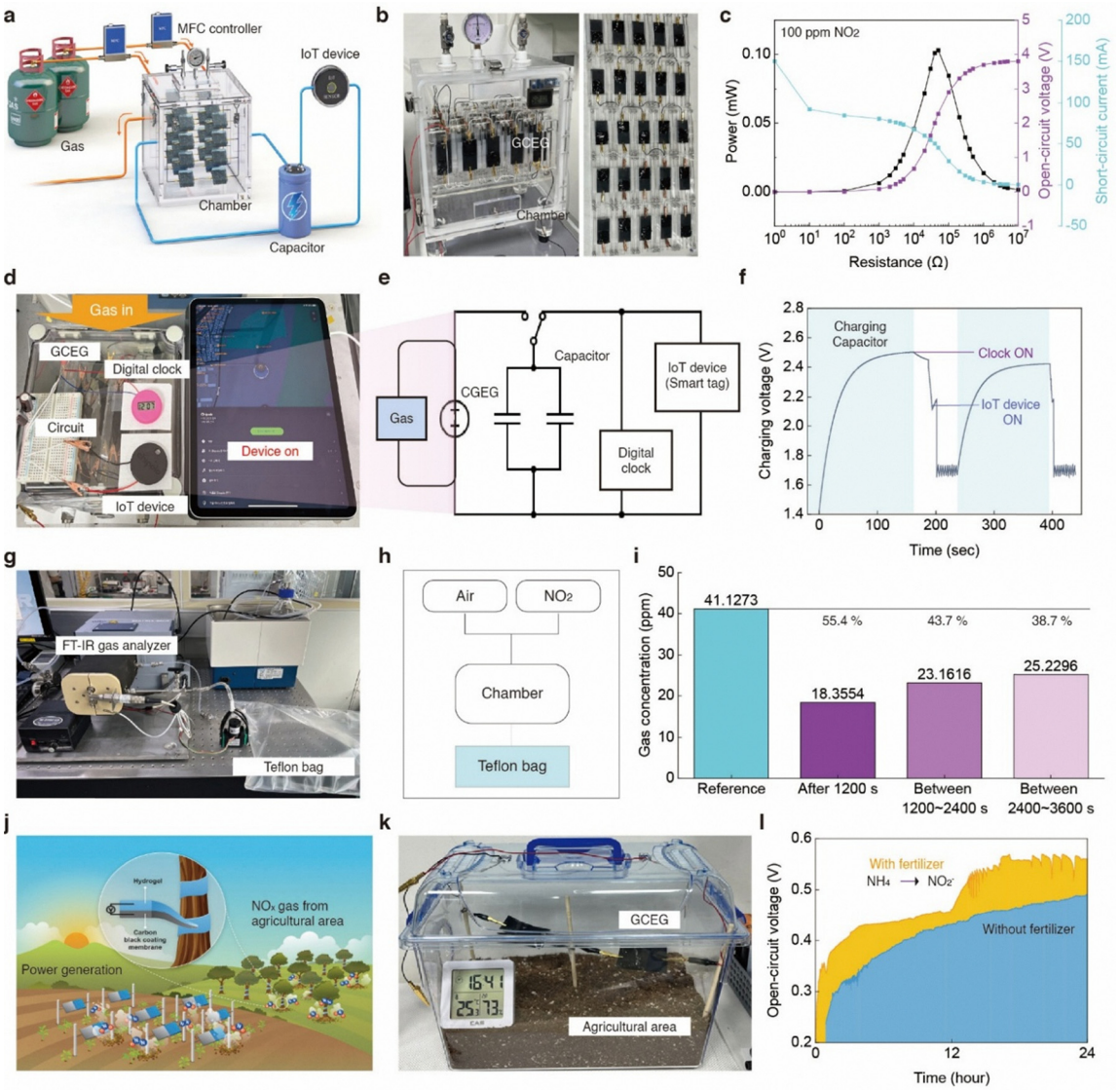

Fig. 5 Scale-up and gas reduction demonstration using the GCEG. (a) Schematic of the setup for the scale-up demonstration, utilizing multiple GCEGs connected in series and parallel. (b) Photograph of the experimental setup showing the array device for increased power output. (c) Variation of the V_{OC}, I_{SC}, and power with external load resistances from 1 Ω to 10 MΩ for an array of 25 devices. (d) Photograph of the setup demonstrating the GCEG powering a Bluetooth location-tracking IoT device. (e) System diagram of the GCEG-powered Bluetooth location-tracking IoT device. (f) Charging voltage profiles when connected to a clock and an IoT sensor. (g) Photograph of the experimental setup illustrating gas reduction by adsorption on the hydrogel in the GCEG. (h) Schematic of the setup used to collect gas samples for concentration analysis. (i) Outlet NO_2 concentration and reduction rates over time, comparing an empty chamber and a chamber containing GCEG devices. (j) Illustration of the GCEG in a real agricultural environment. (k) Simulated agricultural chamber containing the GCEG. (l) Electrical output of the GCEG with and without fertilizer over 24 h.

MFCs. As depicted in Fig. 5b, the array enabled optimization for enhanced power output, with 25 devices arranged in a 5-series/5-parallel configuration. By varying the load resistance from 1 Ω to 10 MΩ, the system delivered a maximum voltage of ~4 V, a current up to 150 μA, and a peak power output of 0.1 mW under 0% RH with 100 ppm NO_2 exposure (Fig. 5c).

Using the scaled GCEG array, we further demonstrated the practical device integration by powering a wearable Bluetooth location-tracking IoT module and a digital clock (Fig. 5d). In this configuration, 18 GCEG devices were connected in a 6-parallel/3-series configuration (Fig. 5e). Under 50 ppm NO_2 at 0% RH, the array charged two parallel-connected 1 mF capacitors (2 mF total) up to ~2.5 V. Connection to the digital clock caused a slight voltage drop, confirming successful operation (Fig. 5f). Similarly, integration with the IoT device triggered sensor activation on a tablet interface, accompanied by a voltage decrease. Additional images are provided in the SI (Fig. S24). Together, these results underscore the feasibility of scaling up GCEG arrays for low-power electronic applications.

In addition, we assessed the gas reduction capability of the GCEG system (Fig. 5g). Outlet gas collected from the chamber system was examined using an FT-IR gas analyzer (Fig. 5h). An empty chamber served as the reference, and outlet gas samples were collected over time as the gas passed through the GCEG array (Fig. 5i). The outlet NO_2 concentration decreased to 18.36 ppm after 20 minutes, corresponding to a 41.1% reduction relative to the reference. The reduction rate gradually declined over time due to site saturation. These findings confirm that the GCEG not only generates electricity but also functions as a gas reduction device through adsorption, indicating its potential for real-world applications.

Finally, we evaluated the electricity generation performance of the GCEG under conditions simulating a natural agricultural environment. In such environments, the use of ammonia-based fertilizers leads to elevated NO_x emissions through the nitrification process (Fig. 5j). To reproduce this scenario, soil mixed with NH_3 fertilizer was placed in a sealed chamber together with the GCEG, and the electrical output was continuously monitored for 24 h (Fig. 5k). Notably, in the presence of fertilizer, a significant voltage increase was observed after 12 h compared to the control without fertilizer, demonstrating that the GCEG can effectively harvest electricity from GHGs generated from natural processes (Fig. 5l). In addition, the GCEG can generate electrical output in real open-field environments when exposed to ambient NO_2, even in the presence of wind and gas diffusion (Fig. S25). These results demonstrate the potential of the GCEG for real agricultural applications.

Conclusions

Based on gas–gel interfacial interactions, we propose a GCEG that simultaneously harvests energy and captures GHGs such as NO_x and CO_2. The device features an asymmetric architecture in which conductive CB-coated mulberry paper is partially covered with a PAM hydrogel. For NO_x, hydrogen bonding between gas molecules and the hydrogel redistributes local electron density, enhancing cation exclusion and modulating the EDL at the electrode interface. This mechanism yields a maximum output of 0.8 V and 55 μA under 50 ppm NO_2. Series and parallel integration increase the output to 4 V and 150 μA, demonstrating the scalability of the device concept. Notably, the integration strategy employed here does not rely exclusively on precisely fabricated, fully reproducible unit devices, but rather serves as a proof-of-concept demonstration that series connection effectively increases the output voltage, without aiming for ideal linear scaling through performance-optimized arrays. By tailoring gas adsorption sites, hydrogels for NO_x and amine-functionalized layers for CO_2, the GCEG enables selective energy harvesting from multiple GHGs. In particular, CO_2-induced electricity generation driven by the amine–CO_2 chemical reaction highlights the feasibility of electricity generation *via* chemical interactions. As a proof-of-concept platform, the present GCEG prioritizes validation of the gas–gel interaction-driven mechanism over full optimization of operational stability and reversibility. Accordingly, humidity-dependent variability, partial loss of adsorption asymmetry under extreme conditions, and incomplete regeneration originate from the current material configuration rather than intrinsic limitations of the device concept. The incorporation of reversible CO_2 capture materials, such as metal–organic frameworks (MOFs) or covalent organic frameworks (COFs), is expected to enable cyclic CO_2 capture–release behavior and overcome the single-use limitation of the current system. Overall, this work introduces a simple, scalable, self-powered platform that integrates gas capture with electricity generation. The gas collected from the system can be further directed to downstream catalytic or electrochemical reactors for detoxification or conversion into value-added products, offering a promising pathway for future GHG utilization.

Methods

Preparation of carbon black-coated mulberry paper

Carbon black (CB) powder (0.1 g) was dispersed in 20 mL of deionized (DI) water containing 0.2 g sodium dodecylbenzenesulfonate (SDBS) as a surfactant. The mixture was sonicated for 1 h to achieve uniform dispersion. Rectangular sheets of mulberry paper (3 × 6 cm^2) were fully immersed in the dispersion for 1 min, removed, and dried in an oven at 65 °C until completely dry. This process was repeated four times to ensure sufficient CB loading. The samples were then dried at 65 °C for at least 12 h before use.

Preparation of polyacrylamide hydrogel

A polyacrylamide (PAM) hydrogel precursor solution was prepared by dissolving 8 g of acrylamide monomer in 90 mL of DI water. Hygroscopic salts were incorporated by adding 7.1 g LiCl and 0.4 g KCl under stirring. Crosslinker and initiator were added sequentially. Specifically, 0.0015 g *N*,*N*′-methylenebisacrylamide (MBAA) and 0.146 g ammonium persulfate (APS)

were introduced. Finally, 550 μL of *N*,*N*,*N*′,*N*′-tetramethylethylenediamine (TEMED) was added to initiate polymerization. The solution was stirred for 10 min at room temperature.

Fabrication of the gas capture and electricity generator (GCEG) device

The GCEG device was fabricated by partially coating the CB-coated mulberry paper with a preformed PAM hydrogel. Specifically, the hydrogel was first synthesized separately to form a soft gel and was then gently stirred to obtain a uniform, sticky gel phase. The mulberry paper was vertically dipped to approximately half its length into the hydrogel mass, allowing the viscous gel to adhere to the exposed surface. Excess hydrogel was removed by slow withdrawal and slight tapping to ensure uniform coverage. The coated samples were left under ambient conditions to stabilize the hydrogel layer on the substrate.

Measurement of gas adsorption capacities

To detect the gas adsorption capacity of the GCEG, we used a gas adsorption analyzer. As NO_2 or CO_2 gas flowed through the adsorption reactor of the GCEG system, variations in gas concentration were measured to evaluate the adsorption capacity and characteristics. The adsorption capacity of the GCEG was determined using the mass balance equation, which was derived from the breakthrough curve that shows changes in concentration. All calculations were performed assuming ideal gas behavior at 298 K and 1 atm.

$$q = \frac{FC_i}{w}\left[t_s - \int_0^{t_s}\left(\frac{C_0}{C_i}\right)dt\right]$$

where q represents the adsorption capacity of the gas (mol g^{-1}), F is the flow rate of the gas entering the reactor (mL min^{-1}), C_i is the initial concentration of the gas in the reactor (ppm), C_0 is the concentration of the gas after adsorption (ppm), w is the mass of the adsorbent (g), and t_s is the time at which the inlet and outlet concentrations become equal (min).

Measurement of electrical properties

The electrical properties of the GCEG devices were characterized using a programmable electrometer (Keithley 6514). The open-circuit voltage (V_{OC}) and short-circuit current (I_{SC}) were recorded under controlled gas exposure conditions. For power output evaluation, an external variable resistor was connected across the device terminals, and the output voltage and current were measured at different load resistances.

Simulation methods

To cost-efficiently describe the PAM hydrogel using an atomistic model, unit cells with more than 20 × 20 × 20 $Å^3$ volumes were introduced by incorporating NO_2, NO, CO_2, H_2 and NH_3 gases and H_2O molecules. A buffer region of at least 20 Å was ensured in all directions to allow for explicit solvation and to avoid interactions between periodic images. Each simulation cell contained 16 gas molecules, representing a deliberately high gas concentration to facilitate the elucidation of gas–hydrogel interaction mechanisms. The equilibrated atomic structures of the PAM hydrogel were obtained through molecular dynamics simulations using the universal force field.[21] Equilibration was performed by alternately applying canonical (NVT) and isothermal–isobaric (NPT) ensembles at 298 K, allowing the system to reach thermal, volumetric, and structural stability.

Based on equilibrated snapshots, a set of electronic structure calculations were performed using SIESTA (Spanish initiative for electronic simulations with thousands with atoms).[22] Strictly-localized numerical atomic orbital (NAO) basis sets were used, with single-ζ plus polarization for hydrogen and double-ζ plus polarization for carbon, oxygen, and nitrogen. The energy cutoff was set to 100 meV. Troullier–Martins-type norm-conserving pseudopotentials[23] were adopted to replace atomic cores. The generalized gradient approximation (GGA) with the Perdew–Burke–Ernzerhof (PBE) functional[24] was employed as the exchange–correlation functional, while van der Waals interactions were treated using Grimme's D3 dispersion correction.[25] The Brillouin zone was sampled using a 2 × 2 × 2 Monkhorst–Pack *k*-point grid.[26] For electronic structure analyses, including charge density difference (CDD) and projected density of states (PDOS), a denser 4 × 4 × 4 *k*-mesh was used. Geometry optimization was performed until the total energy and atomic forces converged to 10^{-4} eV and 0.01 eV $Å^{-1}$, respectively. The net number of electrons transferred to or from the gas molecule upon adsorption (Δe) was calculated as the difference in total Mulliken charges between the adsorbed and gas-phase states: $\Delta e = Q_{gas}^{ads} - Q_{gas}^{iso}$, where Q_{gas}^{ads} and Q_{gas}^{iso} are the total Mulliken charge of the gas molecule in the adsorbed state and isolated state, respectively.

Author contributions

Conceptualization: JSJ and YTG; methodology: JL, HJL, SJK, GM and MC; investigation: MTH, SL, SHK, HJL and GM; visualization: JS, YL, DHL, MTH, SL, SHK, HJL, GM, SW, MC and HWJ; writing – original draft: TGY, HSK, YL and JSJ; writing – review and editing: TGY, HSK, YL and JSJ; supervision: JSJ.

Conflicts of interest

The authors declare no conflicts of interest.

Data availability

All the data generated in this study are included in this article and its supplementary information (SI). Supplementary information: methods, supplementary figures and supplementary tables. See DOI: https://doi.org/10.1039/d5ee06789h.

Raw files or additional data relevant to the paper are available from the corresponding author upon reasonable request.

Acknowledgements

This research was supported by the National Research Foundation (NRF) funded by the Korean government (MSIT) (No. RS-2025-25429261). This research was supported by the GRDC (Global Research Development Center) Cooperative Hub Program through the NRF funded by the Ministry of Science and ICT(MSIT) (RS-2023-00257595). This work was supported by the NRF grant funded by the Korean government (MSIT) (No. RS-2024-00453054). Computational resources were provided by the Korea Institute of Science and Technology Information (KISTI) Supercomputing Center under Project No. KSC-2025-CRE-0414. This research was also supported by the Fundamental Research Program (PNKB010) of the Korea Institute of Materials Science (KIMS).

References

1 L. Aleluia Reis, Z. Vrontisi, E. Verdolini, K. Fragkiadakis and M. Tavoni, *Nat. Commun.*, 2023, **14**, 3581.
2 E. Commission, 2050 long-term strategy, https://climate.ec.europa.eu/eu-action/climate-strategies-targets/2050-long-term-strategy_en.
3 T. E. Müller and W. Leitner, *Beilstein J. Org. Chem.*, 2015, **11**, 675–677.
4 S. A. Montzka, E. J. Dlugokencky and J. H. Butler, *Nature*, 2011, **476**, 43–50.
5 J. N. Galloway, A. R. Townsend, J. W. Erisman, M. Bekunda, Z. Cai, J. R. Freney, L. A. Martinelli, S. P. Seitzinger and M. A. Sutton, *Science*, 2008, **320**, 889–892.
6 U. Skiba and K. Smith, *Chemosphere*, 2000, **2**, 379–386.
7 Z. Wang, Y. Pang, X. Wang, H. Xu, H. Guo, L. Liu, W. Cui and X. Liu, *Carbon Capture Sci. Technol.*, 2025, 100476.
8 N. Mac Dowell, P. S. Fennell, N. Shah and G. C. Maitland, *Nat. Clim. Change*, 2017, **7**, 243–249.
9 T. G. Yun, J. Bae, A. Rothschild and I.-D. Kim, *ACS Nano*, 2019, **13**, 12703–12709.
10 P. Gray and A. Yoffe, *Chem. Rev.*, 1955, **55**, 1069–1154.
11 M. Łukomska, A. J. Rybarczyk-Pirek, M. Jabłoński and M. Palusiak, *Phys. Chem. Chem. Phys.*, 2015, **17**, 16375–16387.
12 R. A. Horne, *J. Phys. Chem.*, 1966, **70**, 1335–1336.
13 A. Hodgson and S. Haq, *Surf. Sci. Rep.*, 2009, **64**, 381–451.
14 J. F. D. S. Petruci, E. Tütüncü, A. A. Cardoso and B. Mizaikoff, *Appl. Spectrosc.*, 2019, **73**, 98–103.
15 U. Kirchner, V. Scheer and R. Vogt, *J. Phys. Chem. A*, 2000, **104**, 8908–8915.
16 H. Zhi, J. Gao and L. Feng, *ACS Sens.*, 2020, **5**, 772–780.
17 J. Wu, Z. Wu, S. Han, B.-R. Yang, X. Gui, K. Tao, C. Liu, J. Miao and L. K. Norford, *ACS Appl. Mater. Interfaces*, 2018, **11**, 2364–2373.
18 Z. Wu, L. Rong, J. Yang, Y. Wei, K. Tao, Y. Zhou, B. R. Yang, X. Xie and J. Wu, *Small*, 2021, **17**, 2104997.
19 J. E. Crooks and J. P. Donnellan, *J. Chem. Soc., Perkin Trans. 2*, 1989, 331–333.
20 C. E. Boyd, *Water Quality: An Introduction*, Springer, 2015, pp. 153–178.
21 C. Casewit, K. Colwell and A. Rappe, *J. Am. Chem. Soc.*, 1992, **114**, 10035–10046.
22 J. M. Soler, E. Artacho, J. D. Gale, A. García, J. Junquera, P. Ordejón and D. Sánchez-Portal, *J. Phys.: Condens. Matter*, 2002, **14**, 2745.
23 N. Troullier and J. L. Martins, *Phys. Rev. B: Condens. Matter Mater. Phys.*, 1991, **43**, 1993.
24 J. P. Perdew, K. Burke and M. Ernzerhof, *Phys. Rev. Lett.*, 1996, **77**, 3865.
25 S. Grimme, S. Ehrlich and L. Goerigk, *J. Comput. Chem.*, 2011, **32**, 1456–1465.
26 H. J. Monkhorst and J. D. Pack, *Phys. Rev. B*, 1976, **13**, 5188.

